Extended Hard X-Ray Emission in Highly Obscured AGNs

Jingzhe Ma[1] , Martin Elvis[1] , G. Fabbiano[1] , Mislav Baloković[2,3] , W. Peter Maksym[1] , and Guido Risaliti[4]
[1] Center for Astrophysics | Harvard & Smithsonian, 60 Garden Street, Cambridge, MA 02138, USA; jingzhe.ma@cfa.harvard.edu, melvis@cfa.harvard.edu
[2] Yale Center for Astronomy & Astrophysics, 52 Hillhouse Avenue, New Haven, CT 06511, USA
[3] Department of Physics, Yale University, P.O. Box 208120, New Haven, CT 06520, USA
[4] INAF—Osservatorio Astrofisico di Arcetri, Largo E. Fermi 5 I-50125 Firenze, Italy

Abstract

Kiloparsec-scale hard (>3 keV) X-ray continuum and fluorescent Fe Kα line emission has been recently discovered in nearby Compton-thick (CT) active galactic nuclei (AGNs), which opens new opportunities to improve AGN torus modeling and investigate how the central supermassive black hole interacts with and impacts the host galaxy. Following a pilot Chandra survey of nearby CT AGNs, we present in this paper the results of Chandra spatial analysis of five uniformly selected non-CT but still heavily obscured AGNs to investigate the extended hard X-ray emission by measuring the excess emission counts, excess fractions, and physical scales. Three of these AGNs show extended emission in the 3.0–7.0 keV band detected at >3σ above the Chandra point-spread function with total excess fractions ranging from ∼8% to 20%. The extent of the hard emission ranges from at least ∼250 pc to 1.1 kpc in radius. We compare these new sources with CT AGNs and find that CT AGNs appear to be more extended in the hard band than the non-CT AGNs. Similar to CT AGNs, the amounts of extended hard X-ray emission relative to the total emission of these obscured AGNs are not negligible. Together with other AGNs detected with extended hard X-ray emission in the literature, we further explore potential correlations between the extended hard X-ray component and AGN parameters. We also discuss the implications for torus modeling and AGN feedback. Considering potential contributions from X-ray binaries (XRBs) to the extended emission, we do not see strong XRB contamination in the overall sample.

Unified Astronomy Thesaurus concepts: Active galaxies (17); X-ray active galactic nuclei (2035); AGN host galaxies (2017)

1. Introduction

Recently, extended hard (>3 keV) X-ray emission, both the hard continuum and fluorescent Fe Kα lines, has been found in several nearby Compton-thick (CT) active galactic nuclei (AGNs) using deep Chandra imaging (e.g., Arévalo et al. 2014; Bauer et al. 2015; Fabbiano et al. 2017, 2018a, 2018b, 2019; Maksym et al. 2017; Jones et al. 2020; Travascio et al. 2021), reaching out from the central supermassive black hole (SMBH) to kiloparsec scales. This emission has consequences for both the feedback of AGNs on their host galaxies and the properties of the central obscuring torus. The hard X-ray emission extends not only in the direction of the ionization cones but also in the region perpendicular to the ionization cones, i.e., cross-cones (e.g., Fabbiano et al. 2018a, 2018b, 2019; Jones et al. 2020). However, in the standard unified model of an AGN, the characteristic hard X-ray continuum and fluorescent Fe Kα lines are confined to the nuclear surroundings because the obscuring torus should completely obscure the nucleus (e.g., Antonucci 1993; Urry & Padovani 1995; Netzer 2015), complicating the determination of the torus properties.

Rather than a completely obscuring torus in the standard unified model of an AGN, the appearance of extended hard X-ray emission supports the increasingly popular scenario of a clumpy structure of the torus (e.g., Nenkova et al. 2008; Elitzur 2012), which allows for the transmission of radiation on kiloparsec scales.

The interactions of the photons escaping the nuclear region with the interstellar medium (ISM) clouds in the host galaxy would give rise to the extended diffuse emission in both the ionization cone and cross-cone directions. For example, the extended hard continuum and Fe Kα emission observed in ESO 428-G014, a well-studied nearby CT AGN, is likely caused by scattering off dense molecular clouds in the host galaxy of photons escaping the nuclear region (e.g., Fabbiano et al. 2018a, 2018b, 2019). The kiloparsec-scale spatial extent is larger at the lower energies, suggesting that the optically thick molecular clouds responsible for the scattering of the higher-energy photons are more concentrated in the inner regions.

The previous discoveries were based on individual objects. We initiated a joint Chandra and NuSTAR survey of nearby heavily obscured AGNs systematically selected from the Swift-BAT spectroscopic AGN survey (BASS; Koss et al. 2017; Ricci et al. 2017) to specifically investigate the extended hard X-ray emission. Our pilot Chandra Cycle 20 survey consists of seven CT AGNs selected from the 70 month catalog (Koss et al. 2017). We quantitatively measured the amount and extent of the extended component above the Chandra point-spread-function (PSF). Five out of the seven CT AGNs show extended emission in the 3–7 keV band detected at >3σ above the PSF, with ∼12%–22% of the total emission in the extended components (Ma et al. 2020). ESO 137-G034 and NGC 3281 display biconical ionization structures with extended hard X-ray emission reaching kiloparsec scales (∼1.9 and 3.5 kpc in diameter). The other three show extended hard X-ray emission above the PSF out to at least ∼360 pc in radius. We further explored potential

Table 1
Observation Log

Source Name	z	ObsID	Instrument	T_{exp} (ks)	PI	Date	Net Counts
NGC 678	0.00946	23808	ACIS-S	37.16	Elvis	2020 Sept 29	401 ± 21
IC 1657	0.01195	23809	ACIS-S	14.33	Elvis	2021 May 19	360 ± 20
NGC 5899	0.00864	23810	ACIS-S	9.57	Elvis	2020 Dec 7	1080 ± 33
NGC 454E	0.01213	23812	ACIS-S	14.33	Elvis	2021 Feb 14	167 ± 13
ESO 234-G050	0.00877	23814	ACIS-S	19.08	Elvis	2021 Mar 14	316 ± 20

Note. The redshifts are taken from NASA-IPAC Extragalactic Database (NED). The total net counts (background subtracted) at 0.3–7.0 keV are listed in the last column.

correlations between the measured quantities with physical parameters such as AGN bolometric luminosity, column density N_H, etc. There appeared to be a moderate correlation between the total extended excess fraction and $\log N_H$ (Ma et al. 2020). However, a definite correlation could not be drawn due to the small sample size. Given that this extended hard X-ray component appears to be relatively common in this uniformly selected sample of CT AGNs, we further discussed the implications for torus modeling and AGN feedback. Detecting hard X-ray emission beyond the traditional dusty torus in the standard unified model of an AGN implies that we need to test and improve torus modeling and update our knowledge of SMBH–host galaxy interactions.

Following the pilot survey, we have been expanding the survey in an effort to build a well-defined statistical sample in order to answer the following questions: (1) What are the typical ranges of extent and amount of extended hard X-ray emission relative to the total emission? (2) What is the origin of the extended hard X-ray emission? (3) What are the implications for AGN models? (4) What are the implications for AGN feedback?

In this paper, we report the results from our Chandra Cycle 22 imaging program on five AGNs that are heavily obscured but not CT, with $23.0 < \log(N_H/\mathrm{cm}^{-2}) < 23.9$. We describe the sample selection, Chandra/ACIS-S observations, and data reduction in Section 2. Section 3 introduces the spatial analysis methods we utilized in this work. We present the results for individual AGNs in Section 4 and compare with other extended hard X-ray-detected AGNs in the literature in Section 5. We also discuss implications for torus modeling and AGN feedback. Section 6 summarizes the conclusions and plans for future observations.

2. Sample Selection, Observations, and Data Reduction

The five heavily obscured AGNs are the targets of our joint Chandra Cycle 22 and NuSTAR program (P.I. M. Elvis). We selected these sources from the Swift-BAT spectroscopic AGN survey 70 month catalog (Koss et al. 2017), based on the following criteria: (1) $z < 0.013$, $D < 50$ Mpc, which gives a plate scale of $1'' \sim 250$ pc, such that the extended emission can be spatially resolved with subarcsecond Chandra ACIS-S imaging; (2) $23.0 < \log(N_H/\mathrm{cm}^{-2}) < 23.9$ from Ricci et al. (2017) to ensure nuclear obscuration is present; (3) 2–10 keV BASS flux of $>4 \times 10^{-13}$ erg cm^{-2} s^{-1} to ensure an adequate count rate.

Table 1 summarizes the Chandra Cycle 22 observations for this work. We first reprocessed the data using CIAO[5] (v4.13)

and CALDB[6] (v4.9.6) (Fruscione et al. 2006), provided by the Chandra X-ray Center (CXC). The default parameters in chandra_repro were adopted. We examined the high background flares, and the entire data set was acceptable. Pileup is not a concern given the low count rates and the (1/4) subarray[7] configurations of our observations.

3. Spatial Analysis Methods

3.1. Subpixel Imaging

We investigated the X-ray morphological properties of the obscured AGNs using the CIAO image analysis tools installed in SAOImage DS9.[8] Images were created in the 0.3–7.0 keV band (full band), the 0.3–3.0 keV band (soft band), the 3.0–7.0 keV band (hard band), and the 6.0–7.0 keV band (where the Fe Kα could dominate) in the following analysis. We employed the subpixel binning technique to push for higher spatial resolution; this has been tested and frequently applied to imaging studies of extended emission and X-ray jets (e.g., Wang et al. 2011a, 2011b, 2011c; Paggi et al. 2012). We used a fine pixel size of $0''062$ (1/8 of the ACIS native pixel size) when producing the images.

3.2. Radial Profiles

To quantitatively measure the extent and amount of extended emission, we generated radial surface brightness profiles in different energy bands and different azimuthal sectors (when possible), following the procedure described in our previous work (e.g., Fabbiano et al. 2017, 2018a; Jones et al. 2020; Ma et al. 2020). We extracted radial profiles using concentric annuli out to a radius of $8''$ for three sources and a radius of $17''$ for two sources, reaching the background level. Off-nuclear point sources within the outer circle were all removed before generating the radial profiles. We started with an annular bin size of $0''5$ and increased the bin size at larger radii to maintain a minimum of 10 counts in each bin. To gauge the magnitude and significance of the extended emission, we compared the radial profiles to the Chandra PSFs for the corresponding energy bands. We modeled the PSF for each given centroid position and energy band using ChaRT[9] and MARX 5.5.0[10] following the CIAO PSF simulation thread.[11] The default

---

[5] CIAO; http://cxc.harvard.edu/ciao/.

[6] CALDB; http://cxc.harvard.edu/caldb/.

[7] We used the central 1/4 subarray (256 rows starting from row 385) at the aim point.

[8] ds9; http://ds9.si.edu.

[9] https://cxc.harvard.edu/ciao/PSFs/chart2/

[10] https://space.mit.edu/cxc/marx

[11] https://cxc.cfa.harvard.edu/ciao/threads/psf.html

Table 2
Excess Counts over the Chandra PSF, Extended Fractions, and Total Excess Fractions

Source Name	Excess Counts $\geqslant 1\rlap{.}''5$	Total Excess Counts	Extended Fraction $\geqslant 1\rlap{.}''5$	Total Excess Fraction
		0.3–3.0 keV		
NGC 678	$35.6 \pm 7.3\ (4.9\sigma)$	$61.2 \pm 9.2\ (6.6\sigma)$	$42.5\% \pm 10.1\%$	$72.1\% \pm 13.9\%$
IC 1657	$42.8 \pm 8.7\ (4.9\sigma)$	$48.2 \pm 9.2\ (5.2\sigma)$	$67.4\% \pm 17.2\%$	$75.9\% \pm 18.7\%$
NGC 5899	< 6.9	$17.0 \pm 8.3\ (2.1\sigma)$	$< 5.3\%$	$9.3\% \pm 4.6\%$
NGC 454E	$5.9 \pm 3.7\ (1.6\sigma)$	$20.9 \pm 6.1\ (3.4\sigma)$	$9.6\% \pm 6.1\%$	$34.0\% \pm 11.0\%$
ESO 234-G050	$49.3 \pm 10.4\ (4.7\sigma)$	$91.3 \pm 12.6\ (7.5\sigma)$	$36.7\% \pm 8.6\%$	$68.1\% \pm 11.7\%$
		3.0–7.0 keV		
NGC 678	$10.9 \pm 5.5\ (2.0\sigma)$	$49.5 \pm 11.1\ (4.4\sigma)$	$4.3\% \pm 2.2\%$	$19.7\% \pm 4.6\%$
IC 1657	$10.0 \pm 7.0\ (1.4\sigma)$	$57.7 \pm 12.6\ (4.6\sigma)$	$3.4\% \pm 2.4\%$	$19.4\% \pm 4.4\%$
NGC 5899	< 22.3	$72.7 \pm 18.6\ (3.9\sigma)$	$< 2.5\%$	$8.1\% \pm 2.1\%$
NGC 454E	< 10.5	$20.3 \pm 7.2\ (2.8\sigma)$	$< 10.0\%$	$19.2\% \pm 7.1\%$
ESO 234-G050	$12.5 \pm 7.5\ (1.7\sigma)$	$31.0 \pm 10.7\ (2.9\sigma)$	$6.9\% \pm 4.2\%$	$17.1\% \pm 6.1\%$
		6.0–7.0 keV		
NGC 678	$5.2 \pm 3.0\ (1.7\sigma)$	$26.9 \pm 6.6\ (4.1\sigma)$	$7.5\% \pm 4.5\%$	$38.7\% \pm 10.6\%$

Note. Extended fraction $\equiv$ (source $1\rlap{.}''5$–$8''$ counts $-$ PSF $1\rlap{.}''5$–$8''$ counts)/(total $8''$ source counts). Total excess fraction $\equiv$ (source $0\rlap{.}''5$–$8''$ counts $-$ PSF $0\rlap{.}''5$–$8''$ counts)/(total $8''$ source counts). We place a 3σ upper limit if there are no excess counts above the PSF (i.e., $< 1\sigma$). For IC 1657 and ESO 234-G050, the outer radius is $17''$.

AspectBlur parameter in *simulate_psf*[12] (blur = $0\rlap{.}''07$) was adopted. The radial profiles show the background-subtracted[13] surface brightness distribution in units of counts per arcsecond^2 in each energy band. The PSF radial profiles were generated in the same energy bands and were normalized to the counts within the central $0\rlap{.}''5$ radius bin.

Following Ma et al. (2020), we take several measures to quantify the amount and extent of the extended emission in each energy band. We first measured the excess counts over the Chandra PSF outside the $1\rlap{.}''5$ radius circle to avoid potential contamination from a nuclear component. We also measured the total excess counts above the PSF, which includes all the extended emission that does not belong to the central point source. Along with the excess counts, we also measured the extended, excess fractions in each energy band. The extended fraction $>1\rlap{.}''5$ is defined as the ratio of the excess counts above the Chandra PSF in the $1\rlap{.}''5$–$8''$ or $1\rlap{.}''5$–$17''$ annular region to the background-subtracted total counts within the $8''$ or $17''$ radius circle at the given energy band. We define the total excess fraction to be the ratio of the total excess counts above the PSF (including the $0\rlap{.}''5$–$1\rlap{.}''5$ region) to the total net counts within the $8''$ or $17''$ radius circle at the given energy band. Table 2 lists the excess counts over the Chandra PSF with associated Poisson statistical errors (including the background error), the fraction of the extended emission in the $1\rlap{.}''5$–$8''$ or $1\rlap{.}''5$–$17''$ annular region, and the total excess fraction in each energy band. In cases where we were able to identify azimuthal sectors, e.g., ionization cones and cross-cones, we also measured excess counts in each sector (Table 3).

In addition to the excess counts and excess fractions, we also estimated the fluxes and luminosities of the extended emission (Table 4). We converted the 0.3–3.0 keV and 3.0–7.0 keV excess counts to fluxes and luminosities assuming an absorbed (Galactic absorption) power-law model with a photon index Γ of

Table 3
Excess Counts over the Chandra PSF in Azimuthal Sectors

Source Name	Sector	Excess Counts $\geqslant 1\rlap{.}''5$	Total Excess Counts
		0.3–3.0 keV	
IC 1657	soft X-ray elongation	$37.9 \pm 7.1\ (5.3\sigma)$	$40.0 \pm 7.4\ (5.4\sigma)$
	cross sector	$4.9 \pm 4.2\ (1.2\sigma)$	$8.2 \pm 4.7\ (1.7\sigma)$
ESO 234-G050	soft X-ray elongation	$46.1 \pm 8.4\ (5.5\sigma)$	$65.4 \pm 9.7\ (6.7\sigma)$
	cross sector	< 15.6	$25.9 \pm 7.3\ (3.5\sigma)$
		3.0–7.0 keV	
IC 1657	soft X-ray elongation	$7.3 \pm 4.9\ (1.5\sigma)$	$24.9 \pm 8.7\ (2.9\sigma)$
	cross sector	< 13.4	$33.5 \pm 8.8\ (3.8\sigma)$
ESO 234-G050	soft X-ray elongation	$10.7 \pm 5.4\ (2.0\sigma)$	$17.3 \pm 7.6\ (2.3\sigma)$
	cross sector	< 13.8	$14.0 \pm 7.1\ (2.0\sigma)$

Note. We place a 3σ upper limit if there are no excess counts above the PSF (i.e., $< 1\sigma$).

1.9 for all the sources. Variations of the assumed Γ from 1.4 to 2.4 change the estimated fluxes/luminosities by less than 20%.

The above-mentioned measurements are based on the simulated Chandra PSF. Potential caveats due to the uncertainties of the simulated PSF are discussed in the Appendix.

We discuss the morphology, extended component, and radial profiles of individual sources in the following section.

4. Results

4.1. NGC 678

NGC 678 is classified as an edge-on, barred spiral galaxy [SB(s)b] at $z = 0.00946$ (NED; $D \sim 42$ Mpc; $1'' \sim 200$ pc) with

---

[12] https://cxc.cfa.harvard.edu/ciao/ahelp/simulate_psf.html
[13] We used annular background regions centered around the targets at $\sim 25''$ (inner) to $\sim 40''$ (outer) in radius, avoiding regions with point sources.
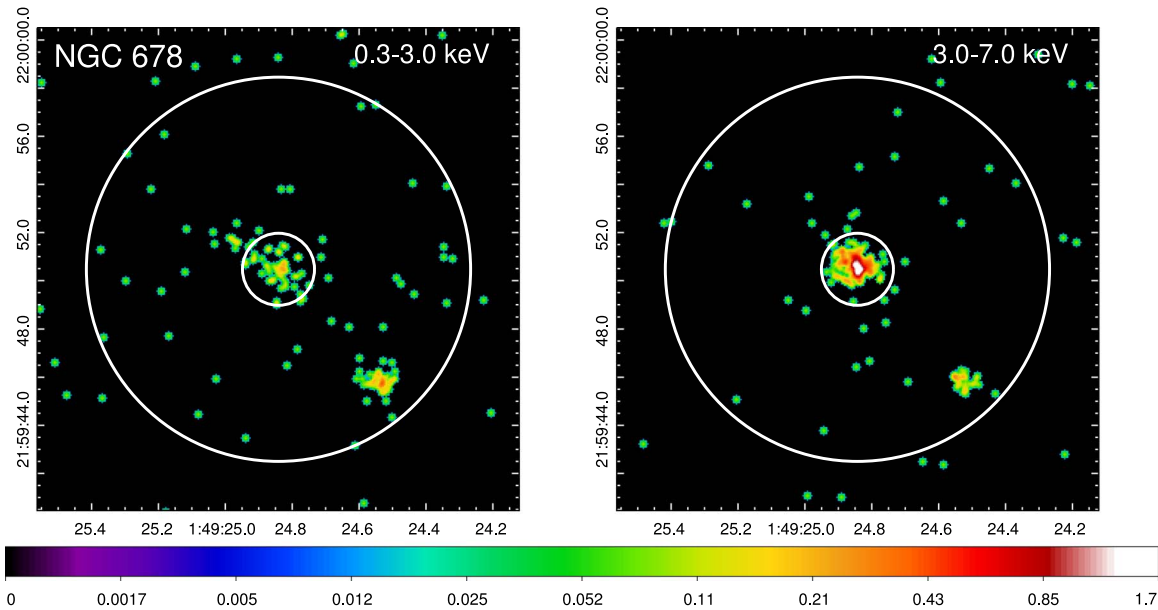
Figure 1. $20'' \times 20''$ Chandra ACIS-S 0.3–3.0 keV (left) and 3.0–7.0 keV (right) band images of NGC 678 at 1/8 subpixel binning (slightly smoothed with a Gaussian kernel of radius = 3 and sigma = 1.5 for better visualization purpose only). The inner $1''.5$ radius circle and the outer $8''$ circle define the region in between for extracting excess counts in the extended emission. All the images are displayed on a logarithmic scale with colors corresponding to the number of counts per image pixel. The off-center X-ray source is excluded from our analysis.

a column density of $\log(N_H/\mathrm{cm}^{-2}) = 23.40^{+0.59}_{-0.50}$ (Ricci et al. 2017).

Figure 1 shows the Chandra images of NGC 678 in the 0.3–3.0 keV and 3.0–7.0 keV bands. The soft X-ray emission appears to be elongated more in the NE–SW direction while the hard band image shows the opposite. An off-center X-ray source is detected $\sim 6''.5$ (~ 1.3 kpc at the galaxy distance) SW of the NGC 678 nucleus with an estimated 0.3–7 keV flux of 4.9×10^{-14} erg s^{-1} cm^{-2} and a luminosity of 9.7×10^{39} erg s^{-1} if associated with NGC 678, which could be an ultraluminous X-ray source (Swartz et al. 2004). However, we cannot completely rule out the possibility that this source is part of an ionization cone structure. This off-center X-ray source is excluded from our following analysis of the extended emission.

As shown in Figure 2, we generate the radial profiles in the full, soft, and hard bands. The soft X-ray emission shows total excess counts well detected at 6.6σ above the PSF out to the outer radius (Table 2). The radial profile of the 3.0–7.0 keV band shows excess emission out to at least $5''.5$ (~ 1.1 kpc) with a total of 49.5 ± 11.1 excess counts detected at 4.4σ, although the excess counts beyond $1''.5$ are not significant (2.0σ). The total excess fraction in the 3.0–7.0 keV hard band is about 20%. We also checked the 6.0–7.0 keV band, and the total excess counts in this band are detected above 3σ although most of the excess counts are in the inner $0''.5$–$1''.5$ region (out to ~ 300 pc).

4.2. IC 1657

IC 1657 is a nearly edge-on ($i = 78°$) barred spiral [SB(s) bc] galaxy at $z = 0.01195$ (NED; $D \sim 53$ Mpc; $1'' \sim 252$ pc) hosting a Seyfert 2 nucleus (Véron-Cetty & Véron 2006) with $\log(N_H/\mathrm{cm}^{-2}) = 23.40^{+0.13}_{-0.09}$ (Ricci et al. 2017). IC 1657 has been studied using optical integral field units (IFUs; Dopita et al. 2015; López-Cobá et al. 2020). Maps of optical emission lines reveal a fan-like extended narrow-line region emerging mainly from one side (E) perpendicular to the highly inclined

Table 4
Estimated Fluxes and Luminosities of the Measured Extended Components

Source Name	N_H (10^{20} cm^{-2})	$f_{0.3-3\mathrm{keV}}$ (10^{-14} erg s^{-1} cm^{-2})	$L_{0.3-3\mathrm{keV}}$ (10^{39} erg s^{-1})	$f_{3-7\mathrm{keV}}$ (10^{-14} erg s^{-1} cm^{-2})	$L_{3-7\ \mathrm{keV}}$ (10^{39} erg s^{-1})
NGC 678	7.57	1.8	3.5	2.9	5.7
IC 1657	2.30	4.0	12.9	8.7	27.8
NGC 5899	1.77	2.2	3.6	16.4	27.1
NGC 454E	2.72	1.7	5.7	3.1	10.1
ESO 234-G050	3.33	5.6	9.6	3.5	6.0
NGC 424	1.76	18.9	58.2	5.8	17.9
NGC 1125	2.73	4.7	12.6	1.6	4.1
NGC 3281	6.49	7.6	19.2	11.4	28.9
NGC 4500	1.05	6.1	14.5	2.6	6.2
ESO 005-G004	11.54	0.7	0.6	2.9	2.5
ESO 137-G034	24.95	11.1	20.0	4.6	8.3
2MASX J00253292 +6821442	51.31	0.4	1.4	1.1	3.5

Note. N_H is the Galactic absorption column density. We assume an absorbed power-law model with a photon index of 1.9.

N–S galactic disk. An ionization cone with an opening angle close to 90° is visible, as revealed by strong [N II] emission (Figure 6 in López-Cobá et al. 2020), extending at least $\sim 11''$ (~ 2.8 kpc) from the plane of the galactic disk. The galactic disk itself is dominated by H II regions as revealed by the Hα emission, while ionized clumps present slightly stronger [O III] emission in the outskirts of the disk (López-Cobá et al. 2020).

Figure 3 shows that IC 1657 has a core of relatively low surface brightness in the soft band, and the soft X-ray emission is elongated and distributed nearly vertically along the N–S
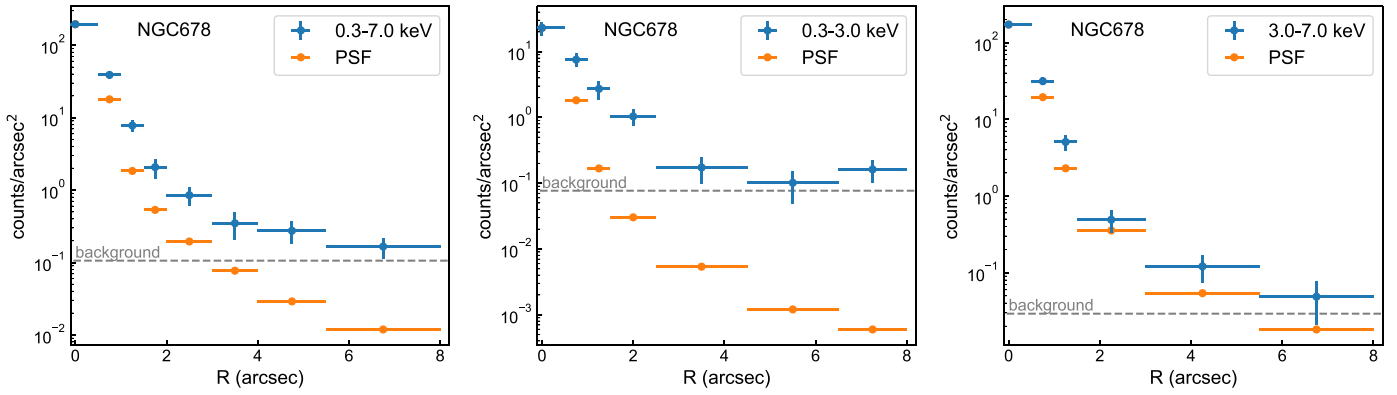
Figure 2. Radial profiles of NGC 678 for the full band, soft band, and hard band. The background has been subtracted from the radial profiles, and its level is indicated by the gray dashed horizontal line. The PSF is normalized to the counts in the central $0\rlap{.}{''}5$ radius bin.
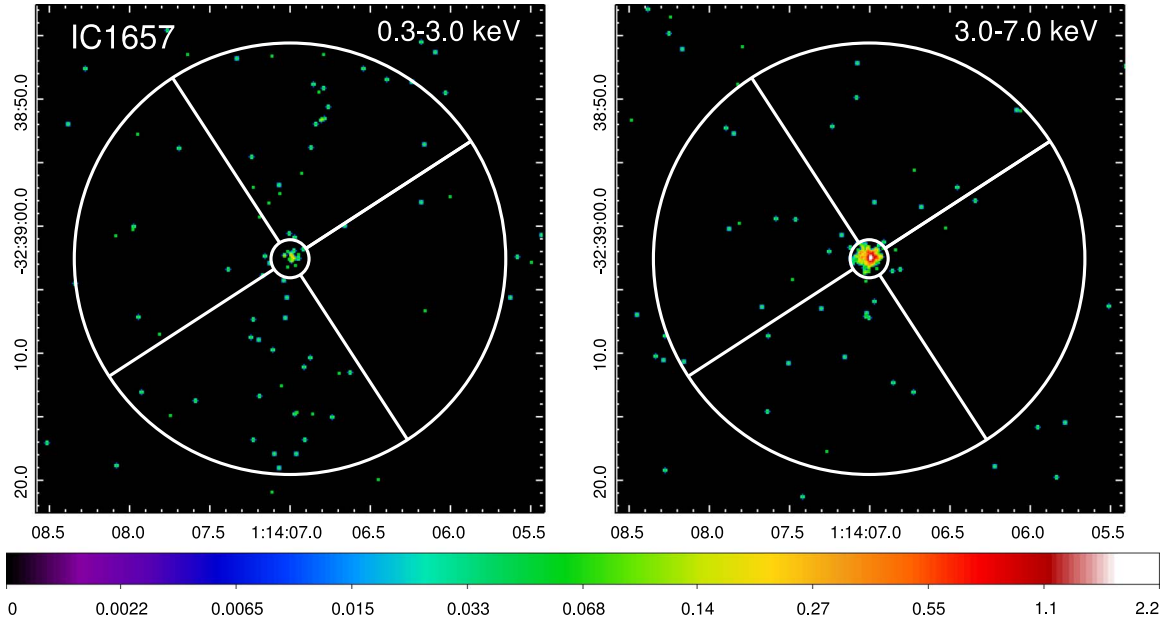

Figure 3. $40'' \times 40''$ Chandra ACIS-S 0.3–3.0 keV (left) and 3.0–7.0 keV (right) band images of IC 1657 at 1/8 subpixel binning (slightly smoothed with a Gaussian kernel of radius = 3 and sigma = 1.5 for better visualization purpose only). The inner $1\rlap{.}{''}5$ radius circle and the outer $17''$ circle define the region in between for extracting excess counts in the extended emission. All the images are displayed on a logarithmic scale with colors corresponding to the number of counts per image pixel.
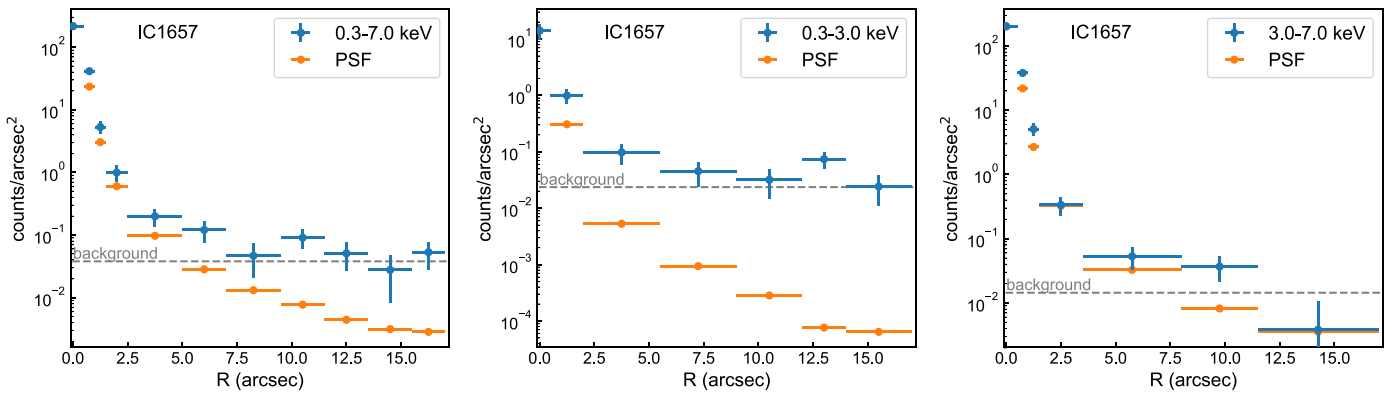
Figure 4. Radial profiles of IC 1657 for the full band, soft band, and hard band. The background has been subtracted from the radial profiles, and its level is indicated as the gray dashed horizontal line. The PSF is normalized to the counts in the central $0\rlap{.}{''}5$ radius bin.

direction, which aligns with the host galactic disk. There is barely any emission in the perpendicular direction. The excess emission in the soft band is well detected (Table 2). The emission in the hard band does not seem to follow the trend in the soft X-rays. IC 1657 has total excess counts of 57.7 ± 12.6 (4.6σ) in the hard band with about 19% of the emission in the
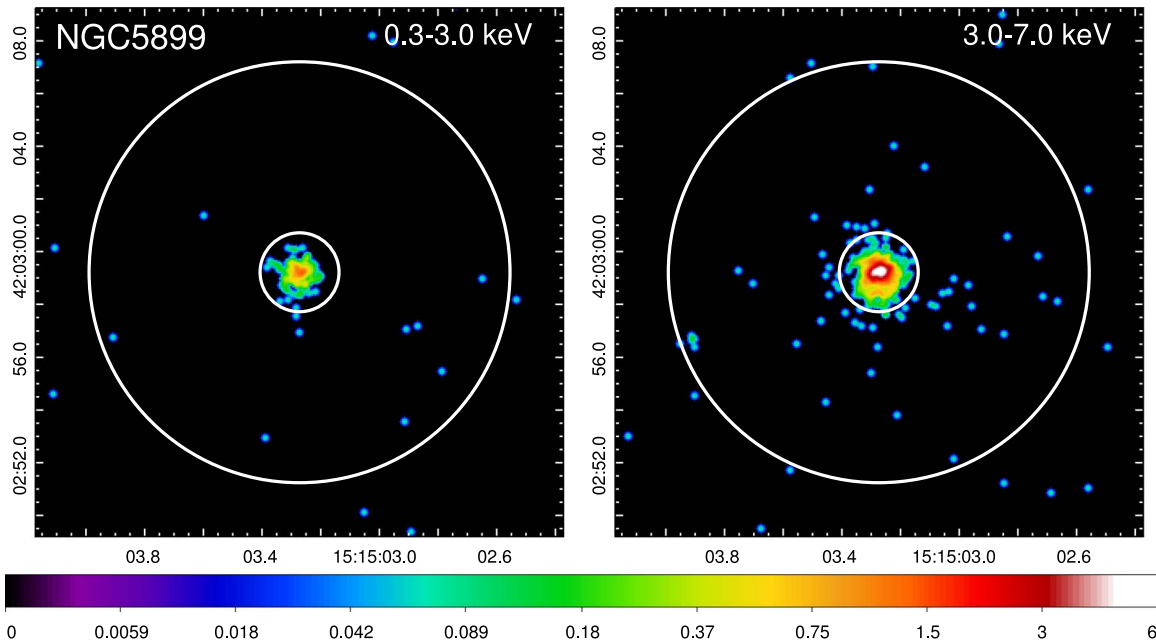
Figure 5. $20'' \times 20''$ Chandra ACIS-S 0.3–3.0 keV (left) and 3.0–7.0 keV (right) band images of NGC 5899 at 1/8 subpixel binning (slightly smoothed with a Gaussian kernel of radius = 3 and sigma = 1.5 for better visualization purpose only). The inner $1''\!.5$ radius circle and the outer $8''$ circle define the region in between for extracting excess counts in the extended emission. All the images are displayed on a logarithmic scale with colors corresponding to the number of counts per image pixel.
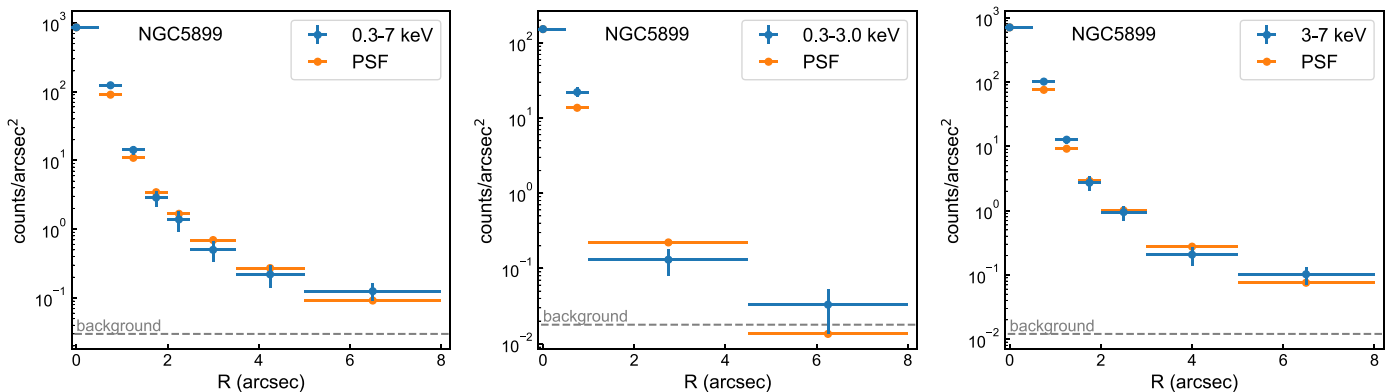
Figure 6. Radial profiles of NGC 5899 for the full band, soft band, and hard band. The background has been subtracted from the radial profiles, and its level is indicated as the gray dashed horizontal line. The PSF is normalized to the counts in the central $0''\!.5$ radius bin.

extended component, but most of the excess emission is found in the inner region out to $1''\!.5$ ($\sim$378 pc) (Figure 4).

Given the strong azimuthal dependence of the soft X-ray emission, we further divided the region into two azimuthal sectors to examine excess emission in these two sectors separately: the soft X-ray elongation sector and the sector perpendicular to it (cross sector). The extended soft X-ray emission is not detected in the cross sector (Table 3). The hard band turns out to have marginally more excess counts in the cross sector, with 33.5 ± 8.8 counts at 3.8σ, than in the soft X-ray elongation direction, with 24.9 ± 8.7 counts at 2.9σ, which is contrary to the soft X-ray morphology.

In most heavily obscured AGNs, an ionization cone is present in soft X-rays whenever an optical ionization cone is visible, and they normally align with each other, but this is not the case in IC 1657. The optical ionization cone appears perpendicular to the soft X-ray extent, which aligns with the H II-dominated galactic disk, and [O III] is found mostly at the

periphery of the star formation region. Instead, as shown earlier, it is the hard X-ray emission that is found perpendicular to, rather than along, the plane of the host galaxy. We will discuss the possible origin of the cone structure and the extended hard X-ray emission in Section 5.

4.3. NGC 5899

NGC 5899 is a barred spiral galaxy [SAB(rs)c] (Ann et al. 2015) at $z = 0.00864$ (NED; $D \sim 38$ Mpc; $1'' \sim 183$ pc) and hosts a Seyfert 2 nucleus (Véron-Cetty & Véron 2006) with $\log(N_{\mathrm{H}}/\mathrm{cm}^{-2}) = 23.03^{+0.04}_{-0.03}$ (Ricci et al. 2017; see also Baloković 2017).

As shown in the Chandra images (Figure 5) and radial profiles (Figure 6), NGC 5899 is the only AGN among this sample that does not show extended soft X-ray emission. In the 3.0–7.0 keV band, there are some excess counts detected at 3.9σ above the PSF with a total excess fraction of $\sim$8%
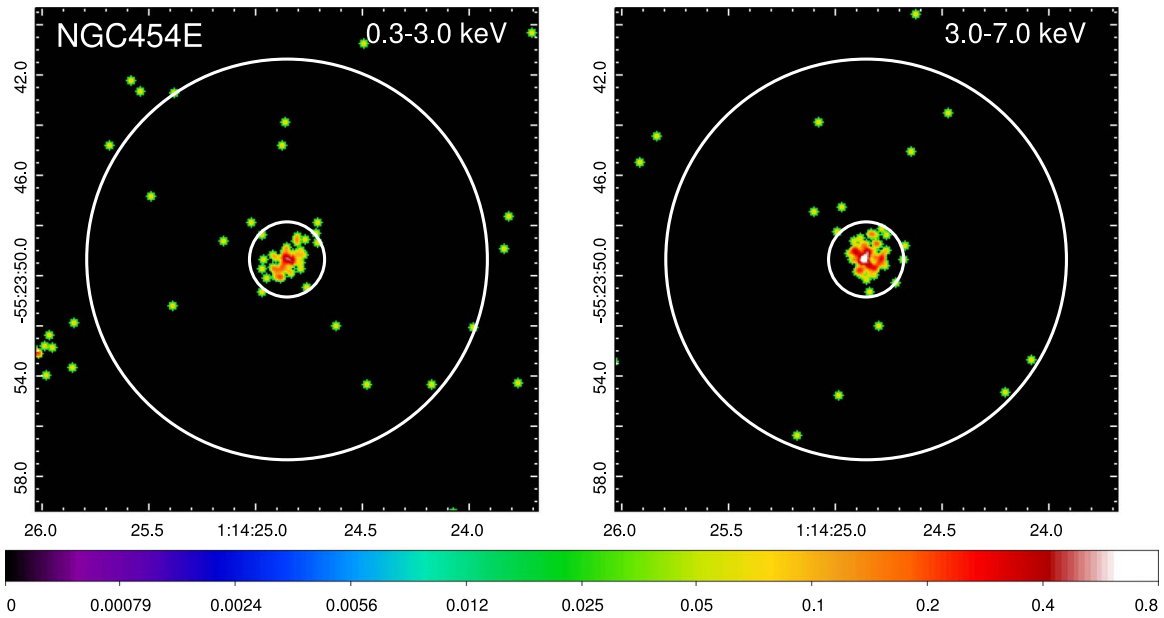
Figure 7. $20'' \times 20''$ Chandra ACIS-S 0.3–3.0 keV (left) and 3.0–7.0 keV (right) band images of NGC 454E at 1/8 subpixel binning (slightly smoothed with a Gaussian kernel of radius = 3 and sigma = 1.5 for better visualization purpose only). The inner $1\rlap{.}''5$ radius circle and the outer $8''$ circle define the region in between for extracting excess counts in the extended emission. All the images are displayed on a logarithmic scale with colors corresponding to the number of counts per image pixel.
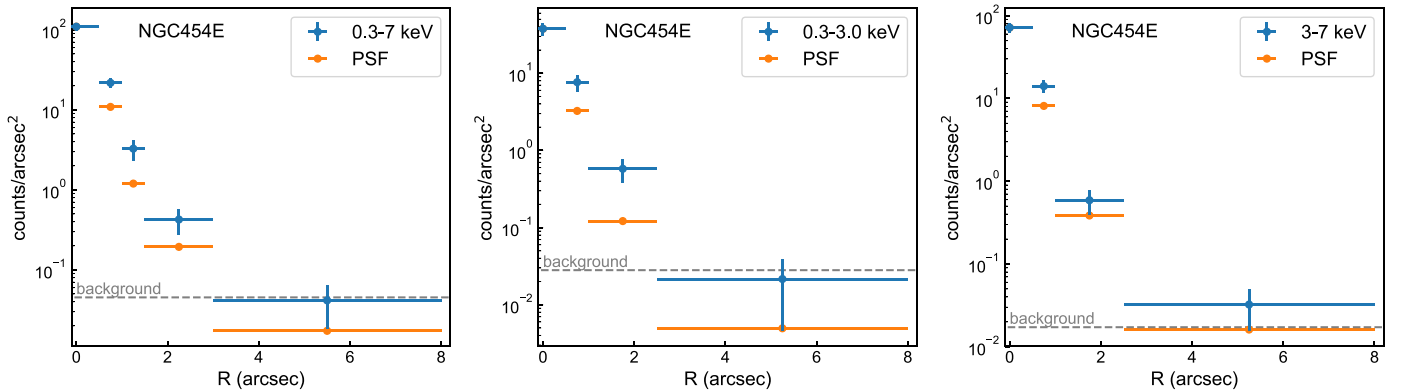

Figure 8. Radial profiles of NGC 454E for the full band, soft band, and hard band. The background has been subtracted from the radial profiles, and its level is indicated as the gray dashed horizontal line. The PSF is normalized to the counts in the central $0\rlap{.}''5$ radius bin.

(Table 2), but beyond $1\rlap{.}''5$ ($\sim$275 pc) the radial profile is basically consistent with the PSF (i.e., no excess emission).

4.4. NGC 454E

NGC 454E is an early-type galaxy at $z = 0.01213$ (NED; $D \sim 54$ Mpc; $1'' \sim 255$ pc) in a pair of interacting galaxies (Johansson 1988; Stiavelli et al. 1998) with $\log(N_{\mathrm{H}}/\mathrm{cm}^{-2}) = 23.30^{+0.04}_{-0.03}$ (Ricci et al. 2017). NGC 454E is also identified as a new member of the class of "changing-look AGNs" (N_{H} varying from $\sim 1 \times 10^{24}$ cm^{-2} to $\sim 1 \times 10^{23}$ cm^{-2}; Marchese et al. 2012; Baloković 2017), i.e., AGNs that show significant variation of the absorbing column density along the line of sight (Matt et al. 2003).

The soft X-ray emission in NGC 454E shows some excess counts above the PSF, mostly in the inner $0\rlap{.}''5$–$1\rlap{.}''0$ region (Figures 7 and 8). In the hard band, there are also some excess counts in the inner $0\rlap{.}''5$–$1\rlap{.}''0$ region but they are not statistically significant, and extended emission beyond $1\rlap{.}''5$ is not detected (Table 2).

4.5. ESO 234-G050

ESO 234-G050 appears to be a low-surface-brightness spiral galaxy[14] ($z = 0.00877$; $D \sim 39$ Mpc; $1'' \sim 185$ pc; NED) in the DECam Legacy Survey imaging (Dey et al. 2019). It hosts a Seyfert 2 nucleus (Aguero 1993; Onori et al. 2017) with $\log(N_{\mathrm{H}}/\mathrm{cm}^{-2}) = 23.08^{+0.12}_{-0.18}$ (Ricci et al. 2017).

ESO 234-G050 exhibits prominent extended soft X-ray emission preferentially distributed along the NW–SE direction as shown in Figure 9, which resembles an ionization bicone structure. The hard X-ray band has a concentrated surface brightness distribution in the center (Figures 9 and 10), but no extended emission is detected above 3σ. Since the soft X-ray emission has a strong azimuthal dependence, we split the data into two azimuthal sectors, one in the NW–SE direction along the soft X-ray elongation and one in the NE–SW direction, to examine excess emission in each sector separately. ESO 234-G050 does not have enough counts for us to produce radial profiles for each

---

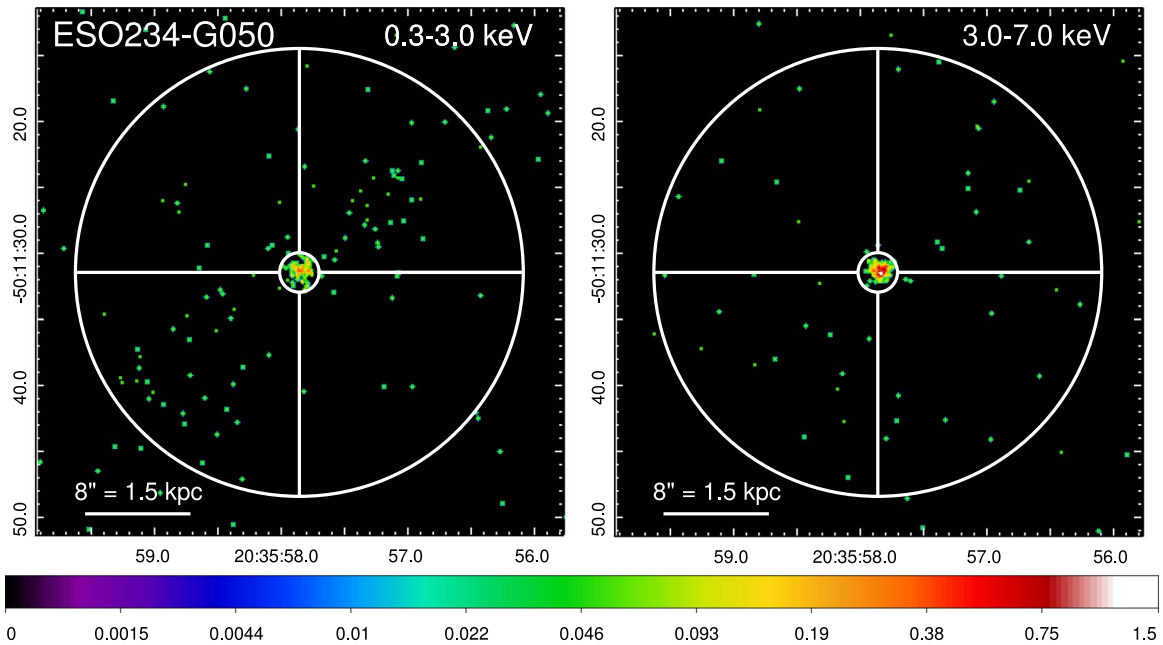[14] ESO 234-G050 was classified as a blue compact dwarf elliptical galaxy by Aguero (1993).

Figure 9. $40'' \times 40''$ Chandra ACIS-S 0.3–3.0 keV (left) and 3.0–7.0 keV (right) band images of ESO 234-G050 at 1/8 subpixel binning (slightly smoothed with a Gaussian kernel of radius = 3 and sigma = 1.5 for better visualization purpose only). The inner $1''.5$ radius circle and the outer $15''$ circle define the region in between for extracting excess counts in the extended emission. All the images are displayed on a logarithmic scale with colors corresponding to the number of counts per image pixel.
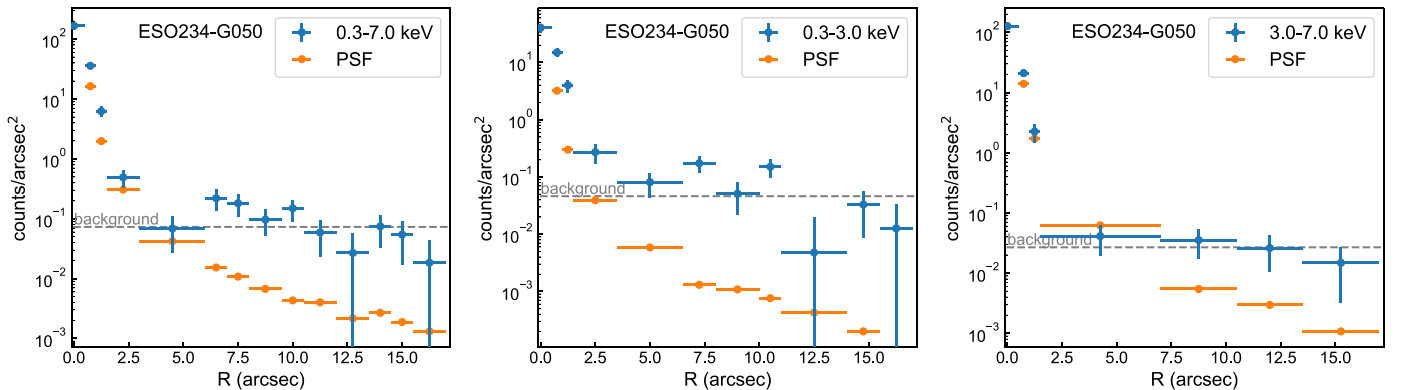

Figure 10. Radial profiles of ESO 234-G050 for the full band, soft band, and hard band. The background has been subtracted from the radial profiles, and its level is indicated as the gray dashed horizontal line. The PSF is normalized to the counts in the central $0''.5$ radius bin.

azimuthal sector though. The extended soft X-ray emission in the soft X-ray elongation sector is well detected as expected. There is also some excess emission detected in the cross sector, mostly in the inner $0''.5$–$1''.5$ region. For the hard band, there are slightly more excess counts in the soft X-ray elongation sector than in the cross sector. However, none of them is detected above 3σ.

5. Discussion

5.1. Potential Contributions from X-Ray Binaries

Could the extended hard X-ray emission be explained by the X-ray binary (XRB) population, which has a fairly hard spectrum? The expected X-ray luminosities from XRBs were estimated by using scaling laws depending upon the dominant XRB populations. In most cases, the X-ray emission is located within the central bulge of the galaxy, where the low-mass XRBs (LMXBs) dominate. Here we used the L_X–L_K scaling relation for LMXBs from Boroson et al. (2011). Since the X-ray emission only occupies the central region rather than the

entire host galaxy, we also corrected the K-band luminosities for the region where X-ray extent is seen ($8''$ or $17''$ circle defined in Section 3), using images from the Two Micron All Sky Survey (Jarrett et al. 2003). For three sources (NGC 424, NGC 1125, and NGC 3281) where the X-ray-emitting region encloses both the bulge and spiral arms where star formation (SF) occurs, we also estimated the expected X-ray emission from high-mass XRBs (HMXBs). We used the scaling relation between L_X and star formation rate (SFR) for HMXBs in Mineo et al. (2012, 2014). The expected HMXB L_X was not corrected for the X-ray-emitting region due to a complex distribution of star-forming regions. These L_X^{HMXB} estimates can then be considered as upper limits. Whenever both the SFR and stellar mass are available, we also derived the expected L_X from the relation with both SFR and stellar mass (Lehmer et al. 2019).

To facilitate comparison with the measured X-ray luminosities in Table 4, we list the expected X-ray luminosities in the 0.3–3.0 keV and 3.0–7.0 keV bands separately in Table 5,
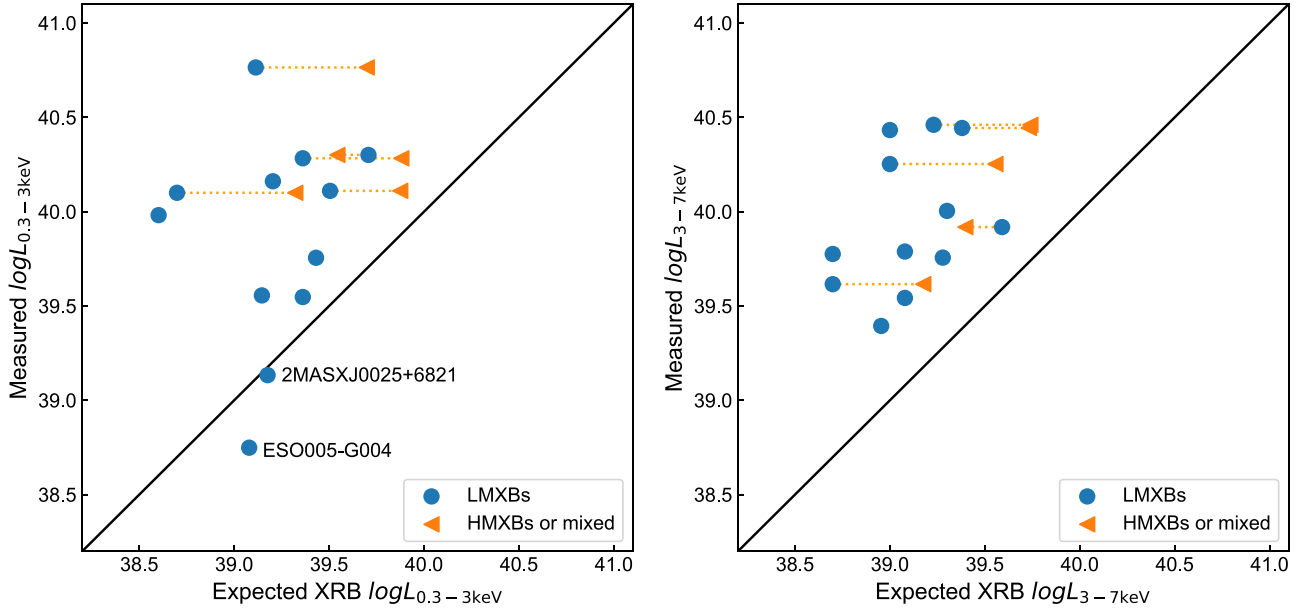
Figure 11. Measured extended X-ray luminosity vs. expected luminosity from XRBs for the 0.3–3.0 keV band (left) and 3.0–7.0 keV band (right). The blue circles are the expected X-ray luminosities from LMXBs. The orange triangles are the expected X-ray luminosities from HMXBs or mixed populations. The dotted lines show the range between the expected $L_X^{\rm LMXB}$ and $L_X^{\rm HMXB/mixed}$. The diagonal line denotes the 1:1 ratio.

Table 5
Expected X-Ray Luminosities from XRBs

Source Name	Morphological Type	$L_{0.3-3\,\rm keV}^{\rm LMXB}$ $(10^{39}$ erg s$^{-1})$	$L_{3-7\,\rm keV}^{\rm LMXB}$ $(10^{39}$ erg s$^{-1})$	$L_{0.3-3\,\rm keV}^{\rm HMXB/mixed}$ $(10^{39}$ erg s$^{-1})$	$L_{3-7\,\rm keV}^{\rm HMXB/mixed}$ $(10^{39}$ erg s$^{-1})$	$r_{0.3-3\,\rm keV}$	$r_{3-7\,\rm keV}$	$f_{3-7\,\rm keV}^{\rm cross-cone}$
NGC 678	SB(s)b; edge-on	2.3	1.9			65%	33%	
IC 1657	SB(s)bc	3.2	2.4	7.5	5.4	25%–58%	9%–19%	13%–29%
NGC 5899	SAB(rs)c	1.4	1.0			39%	4%	
NGC 454E	E	2.7	2.0			47%	20%	
ESO 234-G050	S	0.4	0.5			4%	8%	13%
NGC 424	SB0/a	1.3	1.0	5.0	3.6	2%–9%	6%–20%	
NGC 1125	SB0/a	0.5	0.4	2.1	1.5	4%–17%	12%–36%	
NGC 3281	SAab	2.3	1.7	7.6	5.5	12%–40%	6%–19%	9%–29%
NGC 4500	SBa	1.6	1.2			11%	20%	
ESO 005-G004	Sb; edge-on	1.2	0.9			214%	36%	
ESO 137-G034	S0/a	5.1	3.9	3.5	2.5	18%–26%	30%–47%	45%–70%
J0025+6821	⋯	1.5	1.2			110%	34%	

Note. J0025+6821 is a short name for 2MASX J00253292+6821442. $L_{0.3-3\,\rm keV}^{\rm LMXB}$ and $L_{3-7\,\rm keV}^{\rm LMXB}$ are derived from the scaling relation of LMXBs in Boroson et al. (2011). For NGC 424, NGC 1125, and NGC 3281, $L_{0.3-3\,\rm keV}^{\rm HMXB}$ and $L_{3-7\,\rm keV}^{\rm HMXB}$ are derived from the scaling relation of HMXBs in Mineo et al. (2012, 2014). For IC 1657 and ESO 137-G034, $L_{0.3-3\,\rm keV}^{\rm mixed}$ and $L_{3-7\,\rm keV}^{\rm mixed}$ are derived based on the relation with both SFR and stellar mass from Lehmer et al. (2019). $r_{0.3-3\,\rm keV}$ and $r_{3-7\,\rm keV}$ are the percentage ratios of the XRB expected to the measured $L_{0.3-3\,\rm keV}$ and $L_{3-7\,\rm keV}$, respectively. $f_{3-7\,\rm keV}^{\rm cross-cone}$ is the fraction of the cross-cone excess emission that could be explained by the expected XRBs.

using a typical soft-to-hard ratio of ∼1.3 according to the spectral modeling of XRBs (e.g., Boroson et al. 2011). Figure 11 shows a comparison between the measured extended X-ray luminosities (Table 4) and the expected luminosities from XRBs (Table 5) for both the soft and hard bands.

In all of the sources, the measured extended hard X-ray luminosities are higher than the expected X-ray luminosities due to XRBs by factors of ∼2–25. The X-ray emission from XRBs could well explain some of the hard extents if not all. There is still excess hard X-ray emission that cannot be explained by XRBs, suggesting a connection with the AGN. For the extended soft X-ray emission, the measured luminosities in two sources, ESO 005-G004 and 2MASX J0025+6821,

are consistent with the expected X-ray luminosities from XRBs. For the remaining 10 cases, the excess over the XRB prediction ranges from a factor of ∼1.5 to a factor of 25.

In well-studied CT AGNs, which show spectacular ionization bicones and remarkable correspondence between high-surface-brightness X-ray features and the radio jet and optical line emission, it has been suggested that the extended hard emission is due to scattering in the ISM of photons escaping the nuclear region in the direction of the ionization cone (e.g., ESO 428-G014 (Fabbiano et al. 2017, 2018a, 2018b); IC 5063 (Travascio et al. 2021); see also Jones et al. 2020). The Atacama Large Millimeter/submillimeter Array and SINFONI observations of CO(2–1) and molecular hydrogen (H₂) of ESO
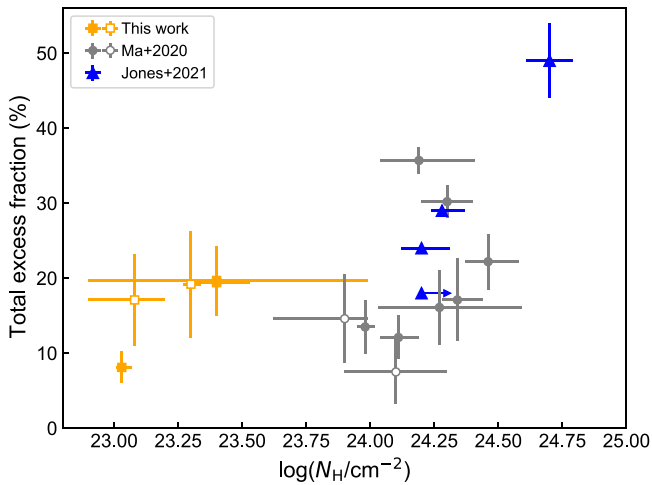
Figure 12. 3.0–7.0 keV total excess fraction vs. logN_H. The orange squares are the five obscured AGNs in this work. The gray circles are the seven CT AGNs plus two individually selected CT AGNs (ESO 428-G014 and NGC 7212) in Ma et al. (2020). For the open squares or circles, the total excess fractions are below 3σ. The blue triangles are the CT AGNs from Jones et al. (2021) with the excess fractions measured in the ionization cone direction.

428-G014 have confirmed that the 3–6 keV continuum and Fe Kα emission are due to scattering from dense ISM clouds (Feruglio et al. 2020).

The hard emission seen in the cross-cone may indicate a porous torus or the predicted hot cocoon around the nucleus due to jet–ISM interaction. XRBs could potentially provide an alternative explanation for the extended hard X-ray emission in the cross-cone direction. Previous well-studied CT AGNs with deep Chandra observations show that the cross-cones account for about 1/3 of the total excess emission in the hard band (Fabbiano et al. 2017; Jones et al. 2021). If we assume the same fraction for this sample (sources in Table 4 that show clear cone-like structures) and also assume half of the expected XRB emission is located in the cross-cone region, then the estimated fractions of the 3–7 keV cross-cone excess emission that could be explained by the expected XRBs are below 30% for three of the sources and up to 70% for ESO 137-G034.

Since most of the extended hard emission cannot be explained by XRBs, we further explore the origin associated with the AGN and compare with other AGNs detected with extended hard X-ray emission in the following sections.

5.2. Comparison with AGNs Detected with Extended Hard X-ray Emission in the Literature

This sample of heavily obscured, though not CT, AGNs was selected under the same criteria as the sample of CT AGNs in Ma et al. (2020) except for the lower absorbing column densities. We also utilize exactly the same metrics to quantify the amount and extent of the extended component. Now we have a larger sample of obscured AGNs with systematically measured excess counts and excess fractions to investigate whether the measured quantities correlate with any physical parameters such as AGN bolometric luminosity L_{bol}, black hole mass M_{BH}, Eddington ratio λ_{Edd}, N_H, etc., which may shed light on the origin of the extended hard X-ray emission.

In Ma et al. (2020), we found a moderate correlation between the total excess fraction and logN_H among the nine CT AGNs (also including ESO 428-G014 and NGC 7212), i.e., CT AGNs with a higher logN_H tend to have a higher total excess

fraction. Jones et al. (2021) presented extended hard X-ray emission from several CT AGNs with accumulatively deep Chandra observations that enable studies of trends in the ionization cone direction versus the cross-cone direction. Jones et al. (2021) found a strong correlation in the ionization cone between the total (hard X-ray) excess fraction and logN_H, while the trend is not observed in the cross-cone region.

Now that we have a larger sample, we add our new sources to Figure 12 to revisit this potential correlation. The orange squares are the five obscured AGNs in this work. The gray circles are the seven CT AGNs plus two individually selected CT AGNs (ESO 428-G014 and NGC 7212) in Ma et al. (2020). The total excess fractions of these AGNs are measured over all azimuthal angles. We also include in Figure 12 the CT AGNs from Jones et al. (2021) with the excess fractions measured in the ionization cone direction. Our sample in this work greatly expands the logN_H parameter space, but there is still a gap at log(N_H/cm^{-2}) $\sim$ 23.5–23.8. The moderate trend in CT AGNs previously observed by Ma et al. (2020) or the strong correlation in the ionization cone observed by Jones et al. (2021) is diluted rather than strengthened by the new sources. We still need more heavily obscured AGNs that cover a wider range of column densities to better probe this relation. The dilution of the trend could also suggest that CT AGNs and non-CT AGNs may have different relations, or there could be a hidden parameter that would separate this sample into subsamples in which the correlation might hold.

No correlations have been found between the total excess fraction and other AGN parameters, i.e., L_{bol}, M_{BH}, or λ_{Edd}. We also use the estimated fluxes or luminosities of the extended components instead of the total excess fraction, and we do not see trends here either.

In addition, we should point out that the Chandra observations of the sources in our survey (the seven CT AGNs in Ma et al. (2020) and the five obscured AGNs in this work) are relatively shallow ($\sim$10–55 ks) compared to those of the previously individually selected CT AGNs (ESO 428-G014 and the five CT AGNs in Jones et al. 2021), which have accumulatively deep observations ($\sim$100–540 ks). Therefore, we should use caution when interpreting results from mixed shallow and deep observations.

Since the seven CT AGNs in Ma et al. (2020) and the five obscured AGNs in this work were systematically selected and observed under the same survey strategies, here we compare these two samples in terms of the detection rate, spatial extent, and total excess fraction of the extended hard X-ray component. In Ma et al. (2020), five out of the seven CT AGNs show extended emission in the 3.0–7.0 keV band detected at >3σ above the PSF. In this sample, we detected the extended hard X-ray emission in three out of the five AGNs. There is no significant difference between the average total excess fractions or fluxes/luminosities of the two samples. However, the sample of CT AGNs, on average, has an apparently larger hard X-ray extent than this non-CT sample. As discussed in Ma et al. (2020) for CT AGNs, the amount of nuclear obscuration may be connected to the dense molecular clouds, i.e., CT clouds, in the host galaxy, which provide the materials needed to scatter the X-ray photons and produce the extended hard X-ray component. The extent of the hard X-ray emission also requires that some of the CT clouds must be coming from much father out in the galaxy than just in the torus. This also explains the observed larger extent in the CT

AGNs than in the non-CT AGNs. Nevertheless we must bear in mind that both samples are still small, and we should revisit this after obtaining large enough samples.

5.3. Implications for Torus Modeling

Although this sample presents a smaller hard X-ray extent than the sample of CT AGNs, these non-CT but still heavily obscured AGNs show hard X-ray emission extending to at least ∼250 pc in radius, which is beyond the traditional dusty torus in the unified model of an AGN (e.g., Urry & Padovani 1995; Ramos Almeida & Ricci 2017). Using a simple formula in Barvainis (1987), we estimated the radius of the outer torus for each of the five obscured AGNs following Ma et al. (2020), and they are all within 60 pc of the nuclei. Also, the amounts of extended hard X-ray emission relative to the total emission of these heavily obscured AGNs are not negligible. Therefore, we should take this component into account to improve torus modeling.

All the AGNs in this sample have high-quality, broadband NuSTAR spectra covering 3–79 keV, which will be presented in a future publication. In principle, the geometry of the obscuring torus such as the scale height, opening angle, inclination angle, and torus covering factor in clumpy torus models (Elitzur 2008; Nenkova et al. 2008) can all be extracted from (e.g., NuSTAR) X-ray spectral modeling (e.g., Murphy & Yaqoob 2009; Baloković et al. 2018; Tanimoto et al. 2019). However, the existence of reprocessed emission on >100 pc scales is currently not accounted for by any published models. Ignoring this new component can lead to biased estimates of the torus covering factor and/or the average torus column density. It is possible to constrain the opening angle from Chandra imaging of the extended X-ray component, and we know the fraction of total emission that belongs to the extended component, which reduces the uncertainties in the remaining torus model parameters.

5.4. Implications for AGN Feedback

About two dozen CT AGNs with prominent biconical narrow-line regions have now been imaged with Chandra (Fabbiano & Elvis 2022). Almost all of these have the bicone intersecting the host galactic disk and interacting with the host ISM, including shocked radio jets and fluorescing molecular clouds, leading to complex X-ray emission regions (Fabbiano & Elvis 2022). They are objects in which we directly see AGN feedback in action.

The conical structure in IC 1657, however, emerges perpendicular to the host plane. What would naturally have been assumed to be an AGN ionization bicone in the soft X-rays turns out to be consistent with the prediction from X-ray binary scaling relations, first found by Fabbiano (1989, 2006). The extended soft X-ray emission has an X-ray luminosity of $L_X \sim 1.3 \times 10^{40}$ erg s^{-1}. The predicted full-band L_X is 1.3×10^{40} erg s^{-1} using the stellar mass and SFR from López-Cobá et al. (2020) and the X-ray/SFR ratio in Lehmer et al. (2019) with ∼40% of L_X in the soft band. In contrast, the hard X-ray emission is more extended in the perpendicular direction, in line with the optical cone. Deeper Chandra data are needed to reveal a potentially more complete hard X-ray morphology.

López-Cobá et al. (2020) conducted Baldwin–Phillips–Terlevich (BPT) mapping of IC 1657 using the MUSE IFU data and found that the spaxels associated with the ionized cone

fall in the region occupied by shock ionization according to the predicated line ratios from theoretical models. The line ratios in the cone region are more compatible with the SF-driven wind rather than AGN-driven wind according to Sharp & Bland-Hawthorn (2010). Therefore they conclude that shock ionization produced by an SF-driven outflow seems to be the most likely explanation for the ionized cone.

The origin of the extended hard X-ray emission in the perpendicular direction is elusive. One possibility is that the hard X-ray emission is still within the galactic disk. There is then plenty of ISM gas for AGN photoionization, or a radio jet[15] to shock against. There also could be molecular clouds for the nuclear photons to interact with, which is the most likely explanation for the extended hard X-ray emission in ESO 428-G014 (Fabbiano et al. 2017, 2018a). If instead the hard X-ray emission extends beyond the galactic disk, as hinted at by the current Chandra data, there would be little material to interact with. IC 1657 could then be an extragalactic analog of the Milky Way Fermi Bubble where the central supermassive black hole probably released vast amounts of energy that powers high-energy jets in the past (Su et al. 2010). Simulations of jet–ISM interactions (e.g., Mukherjee et al. 2018) also describe outflows with hot gas of $kT \gg 1$ keV that do not cool efficiently and might have a low surface density in the hard band. Again, deep Chandra data are required to confirm the extent and reveal a complete morphology of the hard X-ray emission.

The other sources lack multiwavelength data, which inhibits further interpretation. Nevertheless, this newly discovered, extended hard X-ray component opens up a new window to investigating how the supermassive black hole interacts with and impacts the host galaxy.

6. Summary and Conclusions

Following the pilot Chandra survey of nearby CT AGNs, in this work we performed a Chandra spatial analysis of five uniformly selected non-CT but still heavily obscured AGNs to investigate the extended hard X-ray emission by measuring the excess emission counts, excess fractions, and physical scales. Three of these AGNs show extended emission in the 3.0–7.0 keV band detected at >3σ above the Chandra PSF with total excess fractions ranging from ∼8% to 20%. NGC 678 also exhibits extended emission in the 6.0–7.0 keV band, where the Fe Kα line dominates. The extent of the hard emission ranges from at least ∼250 pc to 1.1 kpc in radius for the sample. We estimated the fluxes and luminosities of the extended components for the samples of CT and non-CT AGNs.

We estimated potential contributions from XRBs. In the hard band, XRBs fall short by factors of ∼2–25 in all cases. In 10 cases, XRBs cannot explain the extended soft X-ray luminosity. In two sources, the expected X-ray luminosities due to XRBs could explain the soft extent. XRBs could also provide an alternative explanation to the extended hard emission in cross-cone regions. In most cases, there is still excess hard X-ray emission that cannot be explained by XRBs. Based on deep studies of selected CT AGNs, this emission is likely to be connected with the interaction of the AGN photons with molecular clouds.

We have compared these new sources with CT AGNs in our previous work and find that CT AGNs appear to be more

---

[15] Unger et al. (1989) observed IC 1657 with the Very Large Array in a hybrid B–C configuration but do not show a map of the radio emission (unresolved).

extended in the hard band than non-CT AGNs. We also revisited the tentative correlation found between total excess fraction and $\log N_H$ from the sample of CT AGNs by adding the new sources. However, the trend is diluted by the new sources. We would need AGNs with a wider coverage of $\log N_H$ to further test this relation. It could also suggest that CT AGNs and non-CT AGNs may have intrinsically different relations.

Similar to CT AGNs, the amounts of extended hard X-ray emission relative to the total emission of these non-CT but still heavily obscured AGNs are not negligible. Therefore, this newly discovered component must be taken into account in torus modeling with NuSTAR to avoid biased estimates of the torus covering factor and/or its average torus column density. Our Chandra spatial analysis will reduce uncertainties in torus modeling.

This newly discovered extended hard X-ray component also provides a new opportunity to investigate how the supermassive black hole interacts with and impacts the host galaxy.

Future Chandra observations of a larger sample of heavily obscured AGNs as well as multiwavelength diagnostics are the way to establish this population and fully uncover the origin of this extended component.

Appendix

A.1. Uncertainties in the Simulated Chandra PSF

All the excess emission measurements in this paper are based on the simulated Chandra point-spread function created with the ChaRT optics raytrace tool and the MARX tool that includes detector and aspect effects. The adopted PSF models are the best currently available according to the CXC documentation[16] and to private communications with the PSF experts at the CXC. There are, however, known issues with the simulated Chandra PSF,[16] which could potentially affect the measured excess counts and significance.

A number of the PSF caveats in the CXC documentation[16] are qualitative, not quantitative. As a result, the uncertainties in the excess counts these caveats may introduce in the simulated

PSF are hard to assess. Here we examine the effects on our results due to the documented quantitative PSF uncertainties.

The Chandra PSF consists of a narrow core where specular reflection dominates and an outer core dominated by scattering that falls off roughly as the square of the off-axis angle.[17] We look at the caveats for each part of the PSF in turn.

A.2. PSF Wings ($>10''$)

For energies $>2\,\mathrm{keV}$, the wings of the simulated PSF underpredict the observed surface brightness profile beyond $10''$. The analysis "Wings of the Chandra PSF"[18] shows a comparison between the simulated PSF (SAOSAC) and the observed surface brightness profiles for the 2.4–2.6 keV and 6.4–6.6 keV bands. At 2.4–2.6 keV, the simulated PSF underpredicts the observed surface brightness profile beyond $\sim 20''$. At 6.4–6.6 keV, the difference at $10''$–$20''$ is at most a factor of 2.

Since no studies specifically in the 3–7 keV band are available, we assume a factor of 2 to test for extended excesses above the PSF. For most of our sources, the extended emission does not extend beyond $8''$ in radius, thus is not affected. For IC 1657 and ESO 234-G050, which extend to $17''$ in radius, we estimated the changes in the excess counts in the 3–7 keV band due to this effect. For IC 1657, assuming the simulated PSF counts are a factor of 2 higher, the total excess counts at 3–7 keV decrease by 7.3% (4.2 counts) and the signal-to-noise ratio (S/N) reduces from 4.6σ to 4.2σ. For ESO 234-G050, the total excess counts at 3–7 keV decrease by 6.8% (2.1 counts) and the S/N reduces from 2.9σ to 2.7σ, assuming the simulated PSF counts are a factor of 2 higher.

A.3. Outer Core ($\sim 1''$–$10''$)

According to Figure 11 in the Jerius (2002)[19] PSF memo based on Chandra High Resolution Camera (HRC) data for AR Lac, there are deviations of the model from the data at the $\sim 20\%$ level, albeit with large error bars.

In particular, the four points between $2''$ and $11''$ scatter either side of unity (Figure 11, right) and are clearly inconsistent with a constant value of 1.2, which is the 20% enhancement that we added to the PSF to reassess the significance of the excesses we claim in our objects. The three objects that have 3–7 keV excess counts above 3σ in Table 2 would have reduced significance to 3.2σ for NGC 678, 3.3σ for IC 1657, and 1.0σ (thus nondetection) for NGC 5899, assuming a factor of 1.2 in the outer core. As a caveat, being an HRC observation, the AR Lac data have no energy information and are strongly weighted to energies $<2\,\mathrm{keV}$.

A.4. Inner Core ($<1''$) Artifact

There is also a known asymmetric artifact in the small radial range $0''.6$–$0''.8$ that first appeared around 2002 in the Chandra HRC PSF,[20] and there is evidence that the feature is also present in ACIS data.[20] We used the CIAO tool *make_psf_asymmetry_region* to estimate the level of this asymmetry in the

3–7 keV band, and it remains <6% in all cases. This artifact would not affect the asymmetric cone-like structures at larger radii, >1″. This is especially clear in the cases of IC 1657 and ESO 234-G050.

A.5. Aspect Blur

Another concern is the AspectBlur parameter adopted in the PSF simulation "to avoid pixelization effects in the pseudo-event files."[21,22] We have been using the default blur value of 0″07 in *simulate_psf*. Pixelization effects are not a problem when using subpixel binning. A larger blur of 0″25 has been suggested for ACIS-S observations[21]. As noted,[21] this is "based on a limited set of simulations."

Just three sources were used for the simulations that led to the suggestion of AspectBlur = 0″25.[21,22] Each was believed to be pointlike at the time. One source, AR Lac, was well fit with an AspectBlur of 0″07. AR Lac was observed with the HRC for 20 ks. The HRC oversamples the HRMA PSF. The 0″07 AspectBlur for AR Lac demonstrates that the HRMA optics are not the cause of any blurring. AR Lac also shows that any blurring due to poor aspect solutions is not universal, at least in observations of modest length. Long observations (>50 ks) may be more affected.[23]

The other two sources, RS Ophiuchi and τ Canis Majoris, required a larger AspectBlur ∼0.25″. RS Ophiuchi was observed for 91 ks with ACIS-S (ObsID 7457) and τ Canis Majoris (ObsID4469) was observed for 100 ks with ACIS-I. We checked that the aspect solution did not wander in both observations by dividing them into roughly 20 ks chunks and calculating the offsets of the centroids of each chunk from the first. In no case was the offset larger than 0.08 ACIS pixels, 0″04, and the mean offset was 0.05 ACIS pixels, 0″025. Neither observation contains significant blurring due to aspect errors.

However, both RS Ophiuchi and τ Canis Majoris were later found to be not good point sources. RS Ophiuchi is a symbiotic star with outbursts in 1985, 2006, and 2021. Other symbiotic stars have been found to be extended with Chandra (e.g., Karovska et al. 2010). In fact, RS Oph was found to have variable extended structure following the 2006 outburst (Montez et al. 2022). The third source, τ Canis Majoris, is an O9 star with a strong wind in the rich young cluster NGC 2362 (Stickland et al. 1998). The X-ray emission has been ascribed to interaction with the surrounding ISM (Chlebowski et al. 1989). Moreover, τ Canis Majoris is part of a complex system including a bright O-star companion ∼0″095–0″16 away (Stickland et al. 1998; Maíz Apellániz & Barbá 2020). These properties make τ Canis Majoris a poor prospect for being a point calibration source in Chandra.

In some cases, using a blur of 0″25 produced a wider PSF than the actual data, causing a negative excess (e.g., NGC 5899 in this sample and NGC 424 in Ma et al. 2020). This result is unphysical and so clearly an overestimate. A similar result was found for the double AGN NGC 6240 (Fabbiano et al. 2020).

A.6. An Empirical Consideration

We have five AGNs in our sample, all observed near the optical axis, to ensure the best PSF. Given this strategy, the

PSF is essentially the same in all cases, for a given energy band. Moreover, as shown by the radial profiles, the depths of all the observations are such that we can trace the surface brightness well at least a factor of 10^{-4} from the central bin. If we had detected extensions in all cases, given the uncertainty in the calibration one could have suspected a spurious wing effect. But we do not. In the case where no extent is claimed, the data indeed follow exactly the PSF profile, within statistics. The same is not true for the "extent" cases although the statistics of the observations are similar. This gives us added confidence that our assumptions on the PSF are valid.

A.7. Conclusions

In summary, we do not find supporting evidence for using a larger blur than the default value of 0″07. In the worst-case scenario, where an aspect blur of 0″25 is used in addition to a factor of 2 higher PSF wings and a factor of 1.2 higher in the outer core, we do not detect hard excess emission above 3σ in any cases. We judge this case to be unlikely.

Quantifying the Chandra PSF uncertainties is an incomplete and difficult ongoing effort by CXC and is far beyond the scope of this paper. Even finding appropriate point sources to use as calibrators is hard. For example, tidal disruption events in distant galaxies are surely pointlike to Chandra but, so far, have extremely soft spectra with almost all the counts below 0.5 keV (Auchettl et al. 2017). The release of the Chandra Source Catalog, CXC2.1,[24] will make finding appropriate sources easier.

ORCID iDs

Jingzhe Ma ⓘ https://orcid.org/0000-0003-4178-0800
Martin Elvis ⓘ https://orcid.org/0000-0001-5060-1398
G. Fabbiano ⓘ https://orcid.org/0000-0002-3554-3318
Mislav Baloković ⓘ https://orcid.org/0000-0003-0476-6647
W. Peter Maksym ⓘ https://orcid.org/0000-0002-2203-7889
Guido Risaliti ⓘ https://orcid.org/0000-0002-3556-977X

References

Aguero, E. L. 1993, Obs, 113, 301
Ann, H. B., Seo, M., & Ha, D. K. 2015, ApJS, 217, 27
Antonucci, R. 1993, ARA&A, 31, 473
Arévalo, P., Bauer, F. E., Puccetti, S., et al. 2014, ApJ, 791, 81
Auchettl, K., Guillochon, J., & Ramirez-Ruiz, E. 2017, ApJ, 838, 149
Baloković, M. 2017, PhD thesis, Caltech doi:10.7907/Z9WM1BG8
Baloković, M., Brightman, M., Harrison, F. A., et al. 2018, ApJ, 854, 42
Barvainis, R. 1987, ApJ, 320, 537
Bauer, F. E., Arévalo, P., Walton, D. J., et al. 2015, ApJ, 812, 116
Boroson, B., Kim, D.-W., & Fabbiano, G. 2011, ApJ, 729, 12
Chlebowski, T., Harnden, F. R., & Sciortino, S. 1989, ApJ, 341, 427
Dey, A., Schlegel, D. J., Lang, D., et al. 2019, AJ, 157, 168
Dopita, M. A., Shastri, P., Davies, R., et al. 2015, ApJS, 217, 12
Elitzur, M. 2008, NewAR, 52, 274
Elitzur, M. 2012, ApJL, 747, L33
Fabbiano, G. 1989, ARA&A, 27, 87
Fabbiano, G. 2006, ARA&A, 44, 323
Fabbiano, G., & Elvis, M. 2022, in Handbook of X-ray and Gamma-ray Astrophysics, ed. C. Bambi & A. Santangelo (Singapore: Springer)
Fabbiano, G., Elvis, M., Paggi, A., et al. 2017, ApJL, 842, L4
Fabbiano, G., Paggi, A., Karovska, M., et al. 2018a, ApJ, 855, 131
Fabbiano, G., Paggi, A., Karovska, M., et al. 2018b, ApJ, 865, 83
Fabbiano, G., Paggi, A., Karovska, M., et al. 2020, ApJ, 902, 49
Fabbiano, G., Siemiginowska, A., Paggi, A., et al. 2019, ApJ, 870, 69
Feruglio, C., Fabbiano, G., Bischetti, M., et al. 2020, ApJ, 890, 29

---

[21] https://cxc.cfa.harvard.edu/ciao/threads/marx/#blurring
[22] https://cxc.cfa.harvard.edu/ciao/why/aspectblur.html
[23] https://cxc.harvard.edu/proposer/POG/html/chap5.html#tth_sEc5.4.3

[24] https://cxc.cfa.harvard.edu/csc/about2.1.html

Fruscione, A., McDowell, J. C., Allen, G. E., et al. 2006, Proc. SPIE, 6270, 62701V
Jarrett, T. H., Chester, T., Cutri, R., et al. 2003, AJ, 125, 525
Johansson, L. 1988, A&A, 191, 29
Jones, M. L., Fabbiano, G., Elvis, M., et al. 2020, ApJ, 891, 133
Jones, M. L., Parker, K., Fabbiano, G., et al. 2021, ApJ, 910, 19
Karovska, M., Gaetz, T. J., Carilli, C. L., et al. 2010, ApJL, 710, L132
Koss, M., Trakhtenbrot, B., Ricci, C., et al. 2017, ApJ, 850, 74
Lehmer, B. D., Eufrasio, R. T., Tzanavaris, P., et al. 2019, ApJS, 243, 3
López-Cobá, C., Sánchez, S. F., Anderson, J. P., et al. 2020, AJ, 159, 167
Ma, J., Elvis, M., Fabbiano, G., et al. 2020, ApJ, 900, 164
Maíz Apellániz, J., & Barbá, R. H. 2020, A&A, 636, A28
Maksym, W. P., Fabbiano, G., Elvis, M., et al. 2017, ApJ, 844, 69
Marchese, E., Braito, V., Della Ceca, R., Caccianiga, A., & Severgnini, P. 2012, MNRAS, 421, 1803
Matt, G., Guainazzi, M., & Maiolino, R. 2003, MNRAS, 342, 422
Mineo, S., Gilfanov, M., Lehmer, B. D., Morrison, G. E., & Sunyaev, R. 2014, MNRAS, 437, 1698
Mineo, S., Gilfanov, M., & Sunyaev, R. 2012, MNRAS, 419, 2095
Montez, R., Luna, G. J. M., Mukai, K., et al. 2022, ApJ, 926, 100
Mukherjee, D., Wagner, A. Y., Bicknell, G. V., et al. 2018, MNRAS, 476, 80
Murphy, K. D., & Yaqoob, T. 2009, MNRAS, 397, 1549
Nenkova, M., Sirocky, M. M., Nikutta, R., et al. 2008, ApJ, 685, 160
Netzer, H. 2015, ARA&A, 53, 365
Onori, F., La Franca, F., Ricci, F., et al. 2017, MNRAS, 464, 1783
Paggi, A., Wang, J., Fabbiano, G., et al. 2012, ApJ, 756, 39
Ramos Almeida, C., & Ricci, C. 2017, NatAs, 1, 679
Ricci, C., Trakhtenbrot, B., Koss, M. J., et al. 2017, ApJS, 233, 17
Sharp, R. G., & Bland-Hawthorn, J. 2010, ApJ, 711, 818
Stiavelli, M., Panagia, N., Carollo, C. M., et al. 1998, ApJL, 492, L135
Stickland, D. J., Lloyd, C., & Sweet, I. 1998, Obs, 118, 7
Su, M., Slatyer, T. R., & Finkbeiner, D. P. 2010, ApJ, 724, 1044
Swartz, D. A., Ghosh, K. K., Tennant, A. F., et al. 2004, ApJS, 154, 519
Tanimoto, A., Ueda, Y., Odaka, H., et al. 2019, ApJ, 877, 95
Travascio, A., Fabbiano, G., Paggi, A., et al. 2021, ApJ, 921, 129
Unger, S. W., Wolstencroft, R. D., Pedlar, A., et al. 1989, MNRAS, 236, 425
Urry, C. M., & Padovani, P. 1995, PASP, 107, 803
Véron-Cetty, M.-P., & Véron, P. 2006, A&A, 455, 773
Wang, J., Fabbiano, G., Risaliti, G., et al. 2011a, ApJ, 729, 75
Wang, J., Fabbiano, G., Elvis, M., et al. 2011b, ApJ, 736, 62
Wang, J., Fabbiano, G., Elvis, M., et al. 2011c, ApJ, 742, 23